NASA TECHNICAL NOTE

NASA TN D-4937

C.1

NASA TN D-4937

A FLIGHT MEASUREMENT OF OPTICAL RADIATION FROM SHOCK-HEATED AIR BY USING A TRAILBLAZER II VEHICLE

by Lloyd S. Keafer, Jr., and Ernest E. Burcher

Langley Research Center
Langley Station, Hampton, Va.

NATIONAL AERONAUTICS AND SPACE ADMINISTRATION • WASHINGTON, D. C. • DECEMBER 1968

A FLIGHT MEASUREMENT OF OPTICAL RADIATION FROM SHOCK-HEATED AIR BY USING A TRAILBLAZER II VEHICLE

By Lloyd S. Keafer, Jr., and Ernest E. Burcher

Langley Research Center
Langley Station, Hampton, Va.

NATIONAL AERONAUTICS AND SPACE ADMINISTRATION

For sale by the Clearinghouse for Federal Scientific and Technical Information
Springfield, Virginia 22151 – CFSTI price $3.00

Page Intentionally Left Blank

A FLIGHT MEASUREMENT OF OPTICAL RADIATION FROM SHOCK-HEATED AIR BY USING A TRAILBLAZER II VEHICLE

By Lloyd S. Keafer, Jr., and Ernest E. Burcher
Langley Research Center

SUMMARY

A flight measurement of optical radiation from shock-heated air was obtained by using a Trailblazer II vehicle. Observations in two spectral bands were made near the stagnation point of a high-velocity (6 km/sec) body at extremely high altitudes (80 to 55 km). The reentry body configuration and the reentry velocity allowed observations of nonequilibrium radiation effects not previously measured in flight. Severe truncation and collision limiting were experienced. The measurement results were compared to analytical predictions and previous experiments.

The experiment results complemented those from Project Fire and those from ground-based investigations and can be applied to the problem of reentry heating and to the evaluation of the concept of optically detecting and tracking noncooperative reentry vehicles. The measurement technique used in this experiment, because of its simplicity, may be applicable to other reentry experiments.

INTRODUCTION

The shock-heated air in front of a high-velocity reentry vehicle radiates in the ultraviolet, in the visible, and in the near-infrared parts of the optical spectrum. The spectral intensities of the various radiating species of dissociated air have been observed in ground-based simulations, and the mechanisms of excitation and decay have been studied extensively. Because of their complexity and expense, extensive in-flight experiments have seldom been conducted. The results of a simple flight experiment are described in this paper. The objective was to measure stagnation-point radiation at high altitudes. Particular emphasis was placed on the ultraviolet part of the optical spectrum because its attenuation in the lower atmosphere precluded experimental investigation in previous flight programs.

The payload was accelerated to its reentry velocity by using the five-stage Trailblazer II vehicle. The small conically shaped body attained a reentry velocity of 6 km/sec. The measurements of the radiation from the shock-heated gas were made at altitudes above 55 km. With this body size and shape, reentry velocity, and altitude range,

flight data were obtained on nonequilibrium radiation. The effects of truncation (attenuation of the radiation by protrusion of the body into the shock layer) and collision limiting were observed.

This paper describes the radiation measurement system and presents the flight data. The results are compared to analytical predictions, and conclusions are drawn concerning the spectrum, the overall levels, the degree of truncation, and the degree of collision limiting of the nonequilibrium radiation.

SYMBOLS

r	radius of reentry body, meters
T	temperature in shock layer, degrees Kelvin
t	particle residence time, seconds
u	radiant emittance per unit shock-layer thickness; radiant-energy density, watts/meter^3
V	velocity of reentry body, kilometers/second
δ	distance shock front stands off from reentry body; standoff distance, meters
θ	solid angle of monochrometer (see fig. A-3)
ξ	distance from shock front along streamline, meters
ρ	air density in shock layer, kilograms/meter^3
ρ_∞	free-stream (ambient) air density, kilograms/meter^3
ρ_0	standard (sea-level) air density, kilograms/meter^3
ϕ	acceptance angle of radiometer (see fig. A-3)

CHARACTERISTICS OF SHOCK-WAVE RADIATION

In every shock layer a zone exists directly behind the shock front where the air cannot adjust instantaneously to the new energy conditions and a state of thermal and

chemical nonequilibrium exists. Farther back from the shock front a zone exists where thermochemical equilibrium is approached. Figure 1 is a schematic representation of the thermochemical nonequilibrium and equilibrium zones in a normal shock wave and shows the variations of temperature, density, and radiant-energy density as functions of distance behind the shock front.

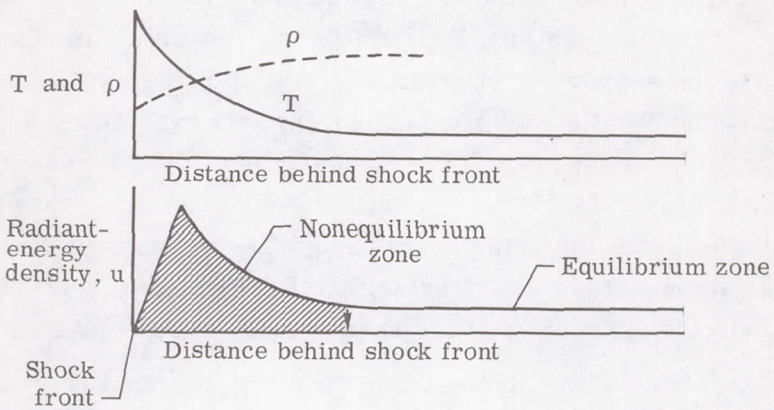

Figure 1.- Radiation zones behind a normal shock front.

A description is given in reference 1 as follows: "Directly behind the shock front very high translational temperatures exist, approaching the values in a perfect gas. The density jump across the shock front is initially close to the perfect gas value. Further downstream, electronic excitation, vibration, dissociation, ionization, and formation of new species take place until the thermochemical equilibrium conditions of the gas are finally reached. During these overlapping processes, loss of energy from the translational mode reduces the translational temperature and the temperature and density approach the equilibrium values. The high temperatures existing near the shock front cause a strong radiation overshoot, as depicted in the figure. There is an excitation time for the radiation to build up to its peak value, believed to be closely related with the time required to populate excited electronic states, and then a relaxation (or decay) time for the radiation to decay to the equilibrium level."

This picture of the radiative process was developed from aerodynamic, thermodynamic, and band-radiation theory, and from the results of many experimental observations. The experiments, being ground based (for example, shock tubes and ballistic ranges), afforded individual control of many parameters, but difficulty was experienced in simulating all conditions of reentry flight. In particular, large reentry bodies could not be tested for extended periods, and high-altitude (low-density) tests, where nonequilibrium radiation predominates, are subject to numerous errors.

EXPERIMENT DESIGN

At the time this flight experiment was conceived, two reentry radiation-measurement programs were being conducted, Project Fire and Trailblazer. Project Fire was designed to investigate the radiant heating problem of large reentry vehicles. The Fire flights employed blunt bodies reentering at velocities greater than 10 km/sec. The radiation observed was mainly from the equilibrium zone (ref. 2). A series of small reentry bodies were flown from Wallops Island, Virginia, by using the Trailblazer vehicle. This vehicle (and the supporting program already in operation) appeared to be the most convenient and economical means for performing this experiment. The reentry bodies used in the Trailblazer program were normally passive and reentered the earth's atmosphere at velocities around 6 km/sec. Ground-based cameras were used to observe the shock-layer radiation from the velocity package. The velocity package (that part of the spacecraft that is accelerated to reentry velocity) consisted of a 12.5-cm spherical rocket motor fitted into the aft section of the reentry body under investigation.

A basic 6^{o} conical body with a 4-cm-diameter hemispherical nose was chosen for this investigation. The complete package was 76 cm long and weighed 9 kg. For this experiment, the Trailblazer velocity package had to be outfitted for onboard measurement of the radiation, since ultraviolet radiation is strongly attenuated in transit through the lower atmosphere. The payload is finally destroyed during reentry so that the data had to be retrieved via telemetry. Part of the experiment consisted of evaluating the performance of a lightweight X-band telemetry system which was capable of penetrating the plasma blackout sheath during the measurement period (ref. 3). Figure 2 is a sketch of the velocity package as designed for this experiment. A discussion of its more important design features follows, and a detailed description appears in appendix A.

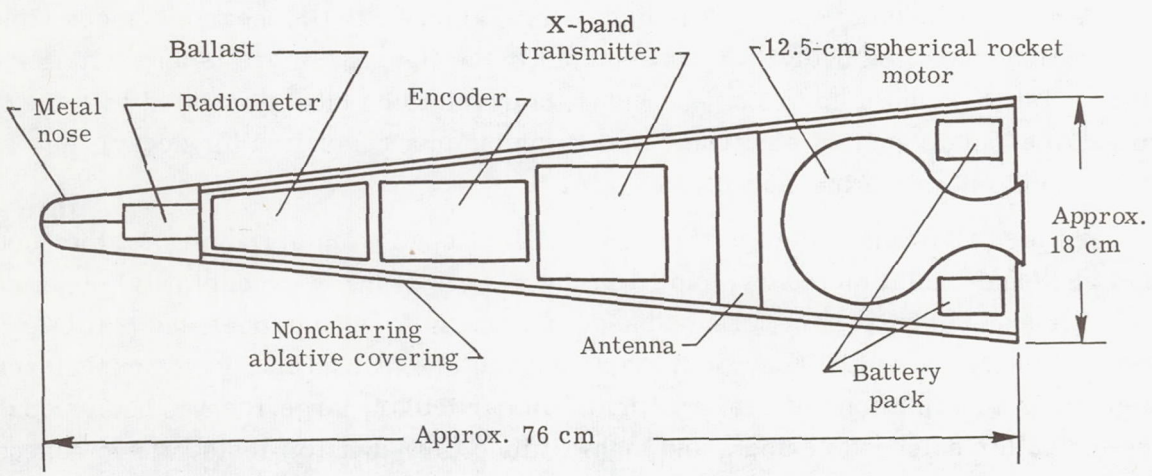

Figure 2.- Velocity package.

In order to view only the radiation from the shock-heated gas, and to avoid the radiation from ablative products, a nonablative nose-cap material was required. This material also had to act as a heat sink to delay its melting (and destruction) so that measurements could be made deeper into the atmosphere. Oxygen-free copper was selected for the nose cap itself; farther back, a noncharring ablative coating was used. The radiometer system, which consisted of two broadband sensors in the copper nose cap, detects the stagnation-point radiation through two solid light pipes. This arrangement was necessary because of the sizes of the sensors and their inability to withstand a high-temperature environment. One detector was sensitive primarily in the ultraviolet, the other in the infrared; high radiation levels were expected in these two spectral bands, but little radiation was expected in the visible region.

Ballast was added to the velocity package to keep its center of gravity well forward for flight stability. The batteries for the radiometer were located in the ballast. The encoder, the X-band transmitter, and the antenna were placed in the larger end of the body where they were adequately shielded from the heat.

Temperature measurements of the nose cap were made at several locations with thermocouples to study the heat transfer and to monitor the light-pipe and sensor environments. The temperature and the performance of the telemeter were also monitored. Details of the fabrication, environmental testing, and calibration of the measurement system are presented in appendix A.

FLIGHT RESULTS

The flight was launched from Wallops Island in May 1965. The velocity package reached an altitude of 300 km and reentered the atmosphere at a velocity of 6 km/sec. The reentry part of the altitude-velocity time history is shown in figure 3. The overall data period lasted about 11 seconds and, as expected, the X-band telemetry delayed radio-frequency blackout until very late in this data period. The telemetry transmitter, however, operated under reduced power during most of the flight because of a partial failure. This partial failure caused some data dropouts, but the measurement instrumentation continued to function properly throughout the flight. The four channels (numbered 10, 11, 12, and 13) of optical radiation data and the three channels (numbered 14, 15, and 16) of temperature data are shown in figure 4. Each of the channels was sampled at the rate of 45 times per second. Some dropouts occur for only one time frame, while others last for as long as 10 frames, thus precluding automatic data reading. The reading is uncertain in the order of 0.5×10^{-3} volt, which is the main source of error in reducing the data.

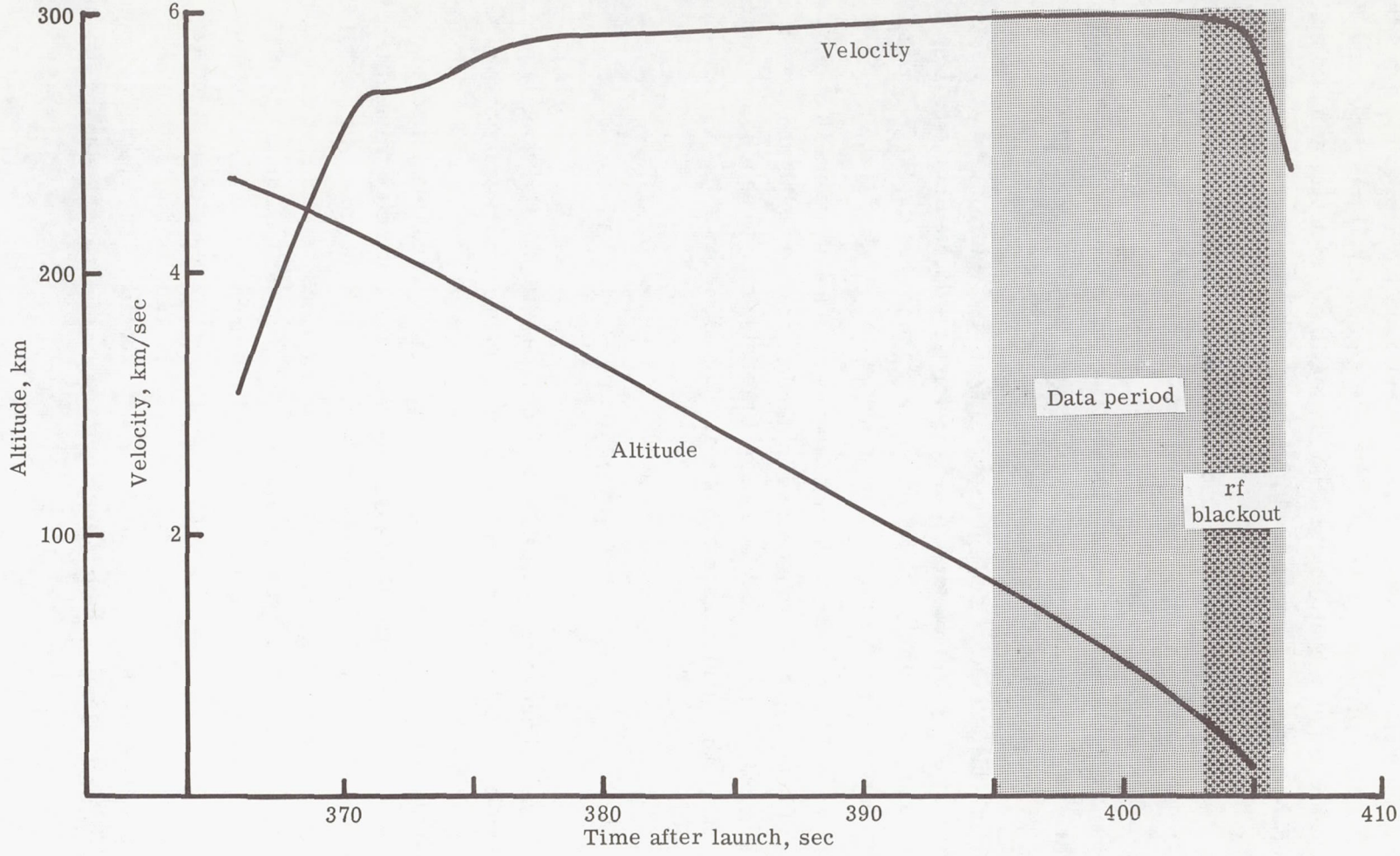

Figure 3.- Altitude and velocity as functions of time (reentry part).

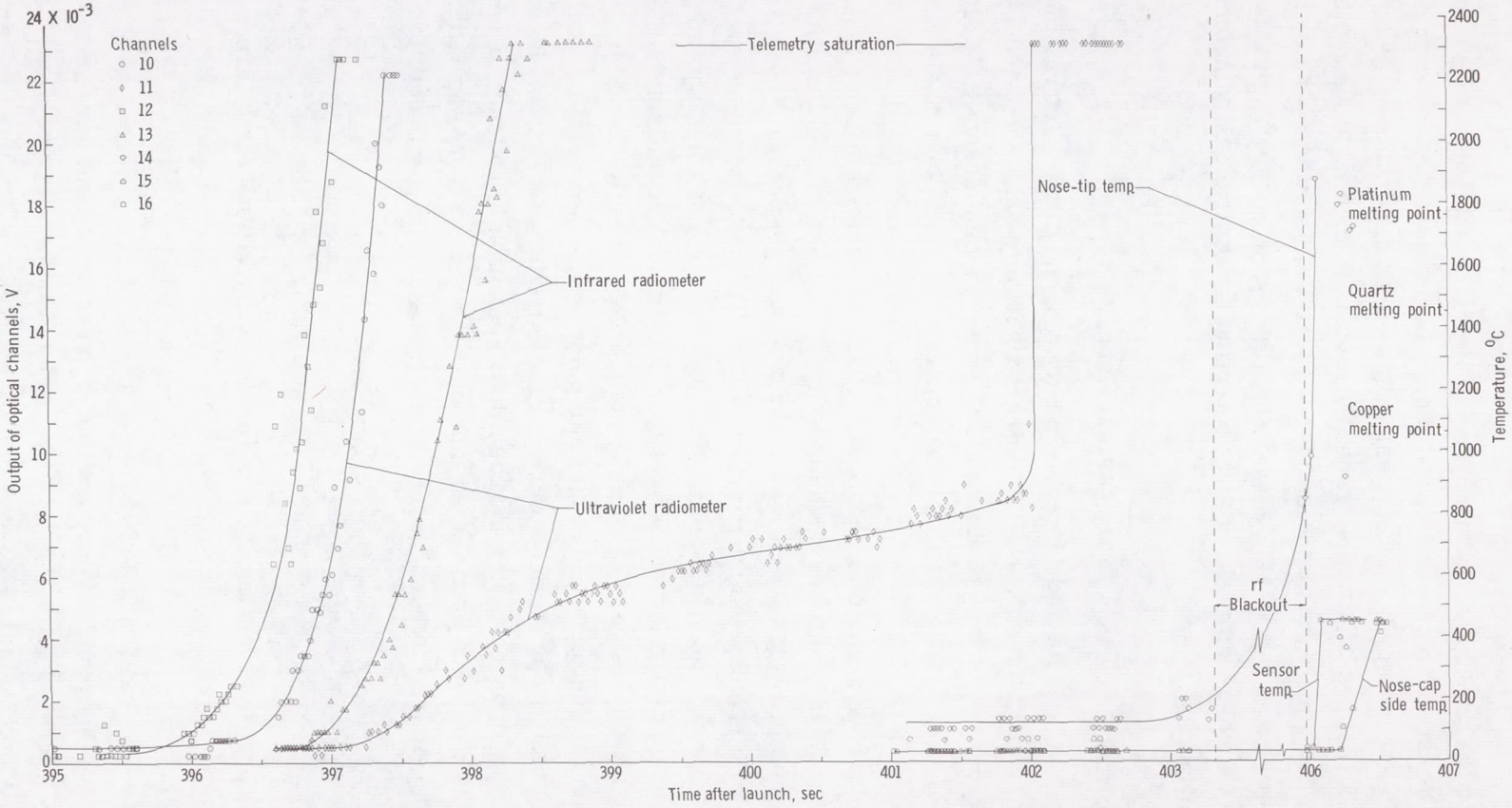

Figure 4.- Nose-cap temperatures and radiometer output voltages as a function of time.

Temperature Data

None of the thermocouple outputs were above the reading noise level prior to 401 seconds. The thermocouple located at the tip of the nose cap between the two light pipes (0.25 cm below the surface of copper) indicated a temperature rise to the melting point of copper in the next 5 seconds. The thermocouple located along the side of the nose cap and the one located near the optical sensors indicated temperature rises only after the blackout period was over. Apparently, the copper nose cap performed well its function of delaying nose-cap melting and protecting the optical instrumentation during the measurement period.

Optical Data

Telemetry channels 10 and 11 read the output of the ultraviolet radiometer, while channels 12 and 13 read the output of the infrared radiometer. The attenuation was adjusted so that channel 10 was 20 times more sensitive than channel 11; similarly, channel 12 was 17 times more sensitive than channel 13. The end of the usable data period occurred when the telemetry channels saturated, nominally at 20 mV. The data period for the infrared radiometer (channels 12 and 13 combined) lasts less than 3 seconds, ending around 398.3 seconds. The data period for the ultraviolet radiometer (channels 10 and 11 combined), however, lasted almost 4 seconds longer. For this added time the slope of the voltage curve is smaller, except at 402 seconds, where the curve abruptly jumps to the telemetry saturation level. Possible deleterious effects responsible for this anomalous action are discussed subsequently. The small fluctuations in the data (beyond what can reasonably be assigned to reading error) are probably caused by the body spin and coning motions which move the stagnation point off the geometric center line away from the light pipes. (Body motions were not measured.) Because of the anomalies caused by telemetry dropouts, body motions, and the action of channel 11 beyond 398.5 seconds, the data have been faired, and only the period from approximately 396 to 398 seconds is considered in subsequent comparisons to analytic predictions and other measurements.

Reduction of Optical Data

All field calibrations during the prelaunch period satisfactorily repeated (within ±5 percent) the initial field calibration which was made immediately after the laboratory calibrations. The primary (laboratory) calibrations used to reduce the data are shown in figures 5 to 8. The calibration of the solid angles of acceptance (fig. 5) and the calibration of the absolute spectral response (fig. 6) were done simultaneously by using intense sources, a special diffusing element, and a standard thermopile. The spectrum for the nonequilibrium radiation anticipated for the flight conditions is discussed in

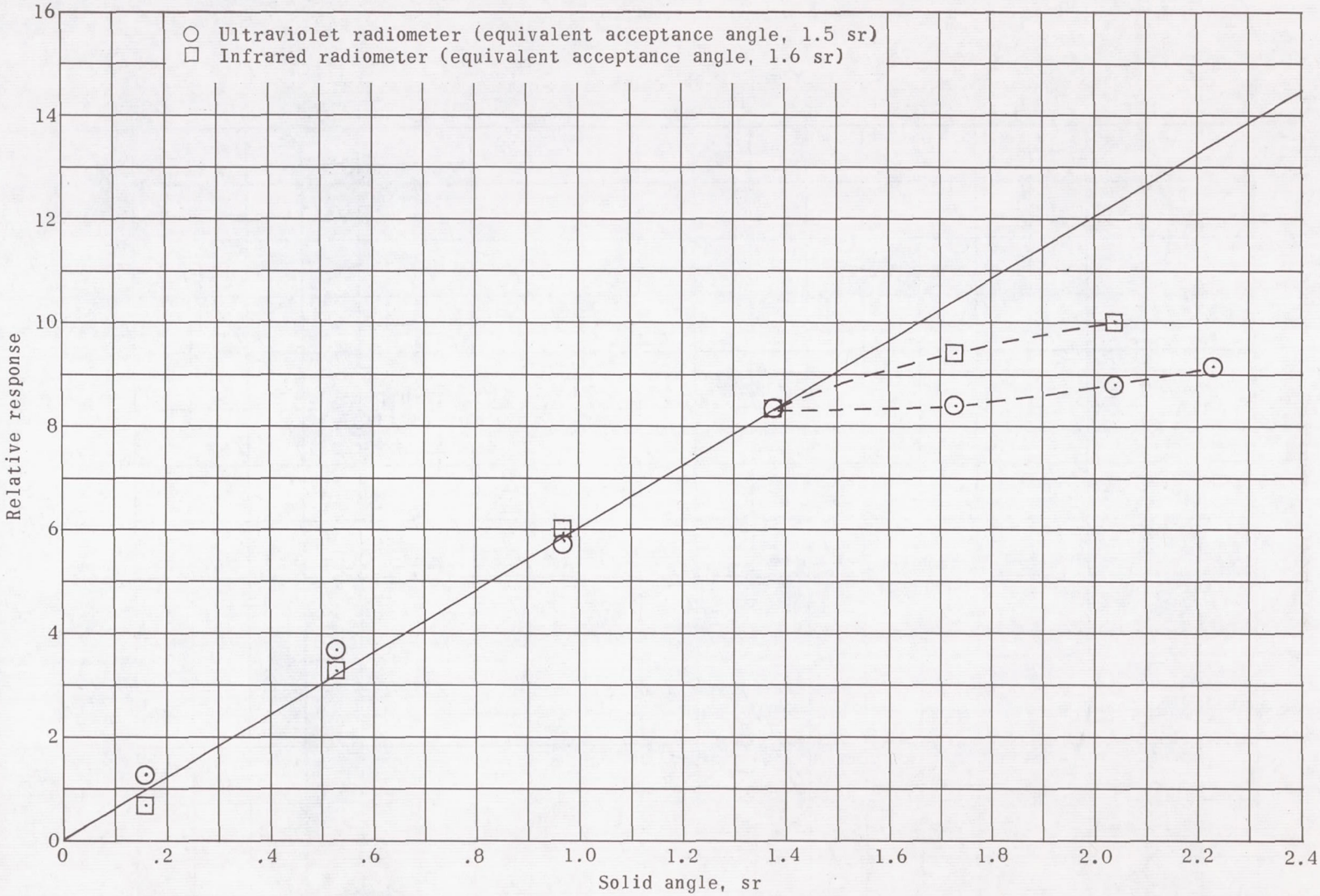

Figure 5.- Acceptance angles of radiometers.

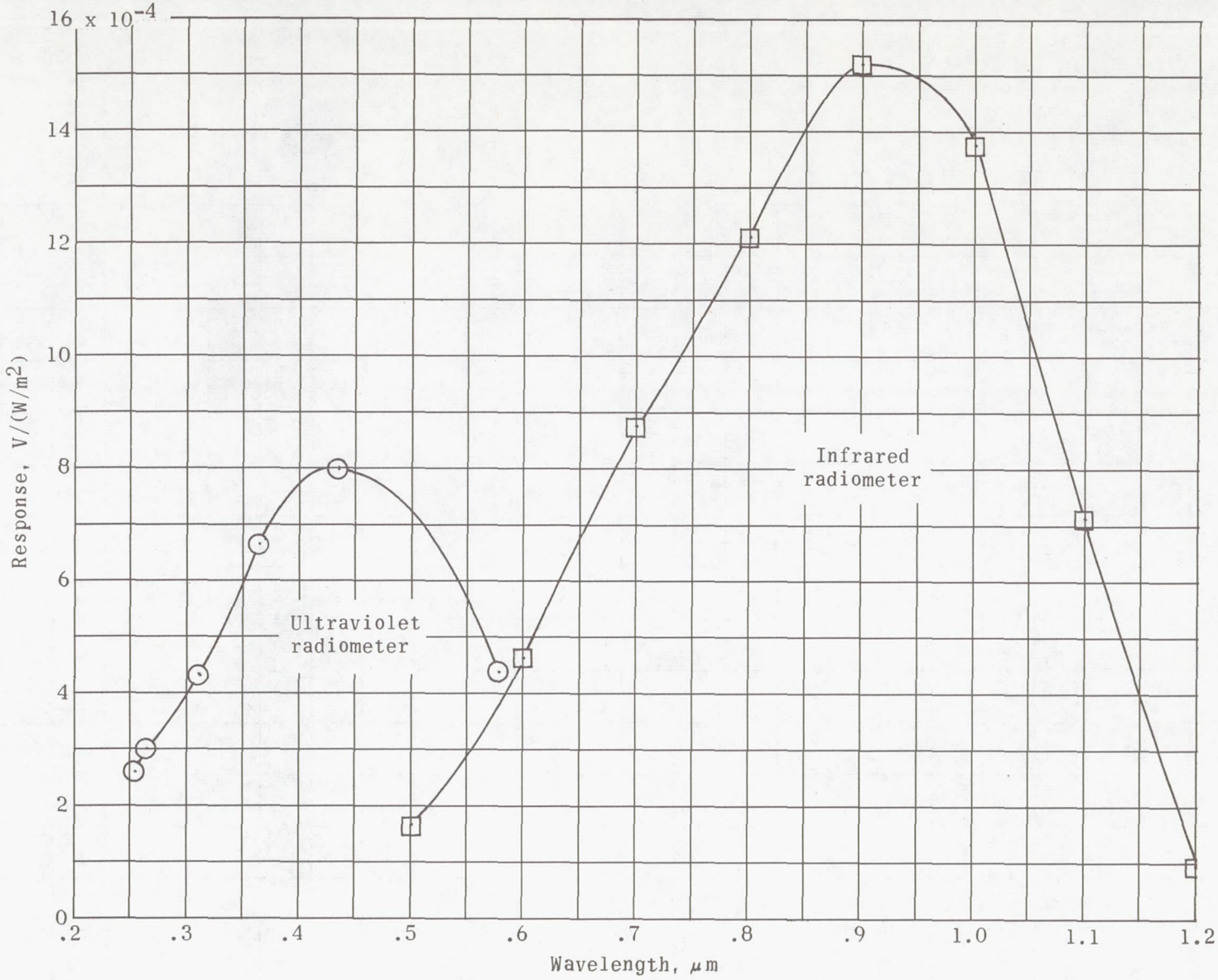

Figure 6.- Spectral calibration.

appendix B and is shown in figure 7. This spectrum was used with figure 6 to derive the calibration curves (fig. 8) for the two radiometers in their respective spectral bands. The dashed-line parts of these curves represent radiation levels anticipated in flight which could not be produced in the laboratory. (Details of the calibration procedure are given in appendix A.) By using these calibration curves the measured voltages from figure 4 were converted to shock-layer radiances in watts/meter^2-steradian in the two spectral bands. Since very little radiation was expected in the region of the overlap of two radiometers and in the region outside their combined spectral band, the two radiances were summed directly to obtain the total radiance. These results are plotted in figure 9 and are discussed and compared to analytic predictions and to other measurements in the subsequent section.

DISCUSSION OF RESULTS

As described previously, the density and temperature conditions of the shock layer give rise to vibrational excitation, dissociation, and ionization of the gas, and to the formation of various radiating species. In the nonequilibrium zone the density and temperature conditions change rapidly with distance from the shock front (fig. 1), and the radiation profile also shows rapid changes. In the equilibrium zone farther back from the shock front the conditions stabilize, and the radiation becomes nearly constant with distance from the shock front.

In order to compare the flight results to analytical predictions and other observations, the relative contribution from the two zones must be determined. Normal shock-wave theory predicts that the equilibrium radiation will have a larger ultraviolet component and will predominate at free-stream densities representative of altitudes below 30 km (refs. 4 to 7). At the lower densities (altitudes above 42 km) the nonequilibrium radiation should predominate. Furthermore, aerodynamic theory predicts that at the high altitudes a nonblunt body will protrude into the bow shock layer far enough to truncate effectively the whole equilibrium zone. Calculated predictions of the equilibrium radiation are given in appendix B. A comparison of the calculated predictions (spectrum and nontruncated level) to the flight results supports the thesis that equilibrium radiation is negligible for the low-density conditions experienced throughout the whole measurement period.

In order to make the comparison of the flight results to nonequilibrium radiation predicted by theory and other observations, the following approach was taken:

(1) Derive an anticipated spectrum from theory and experimental observations. Compare the contributions in the two spectral bands.

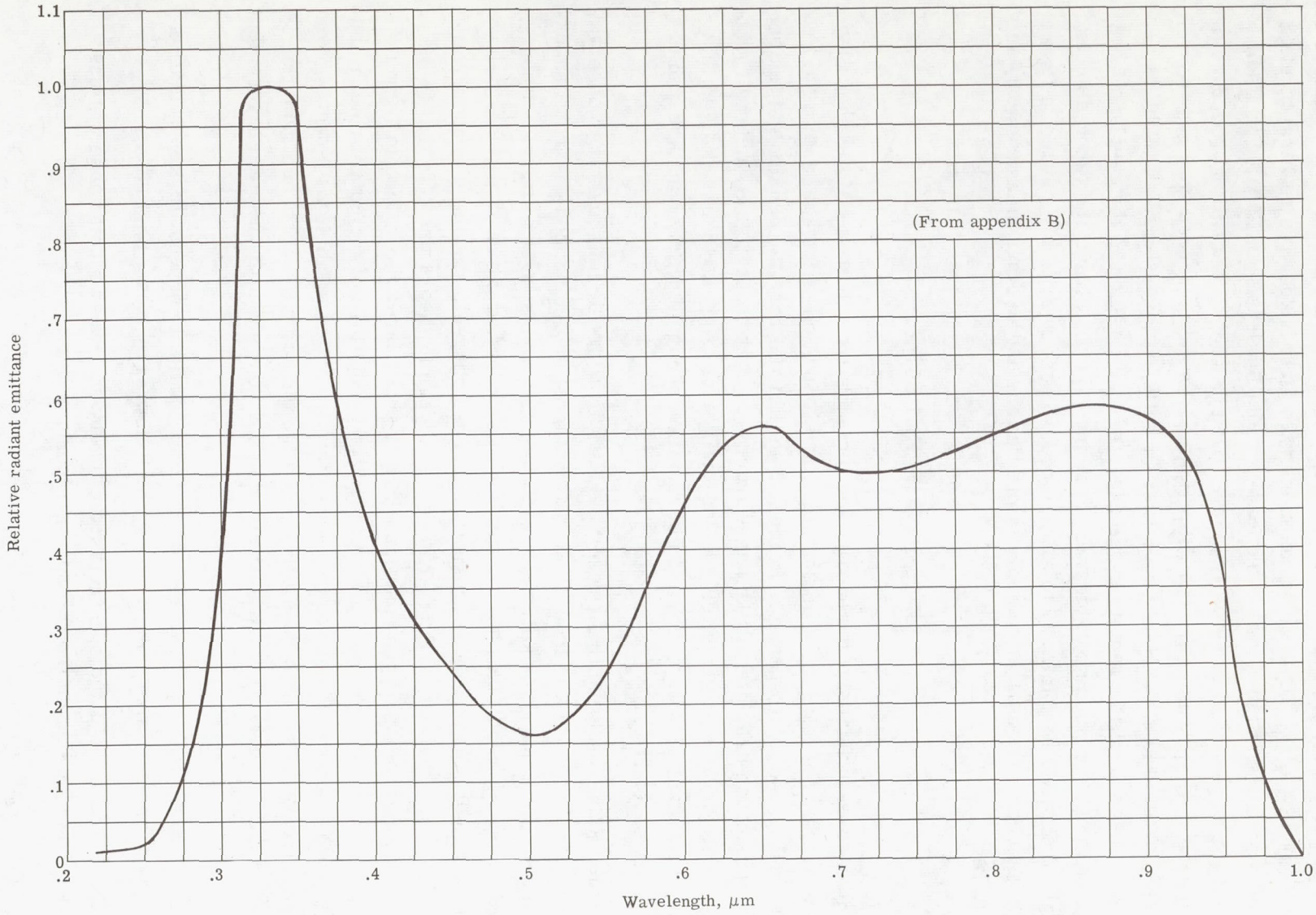

Figure 7.- Anticipated spectrum.

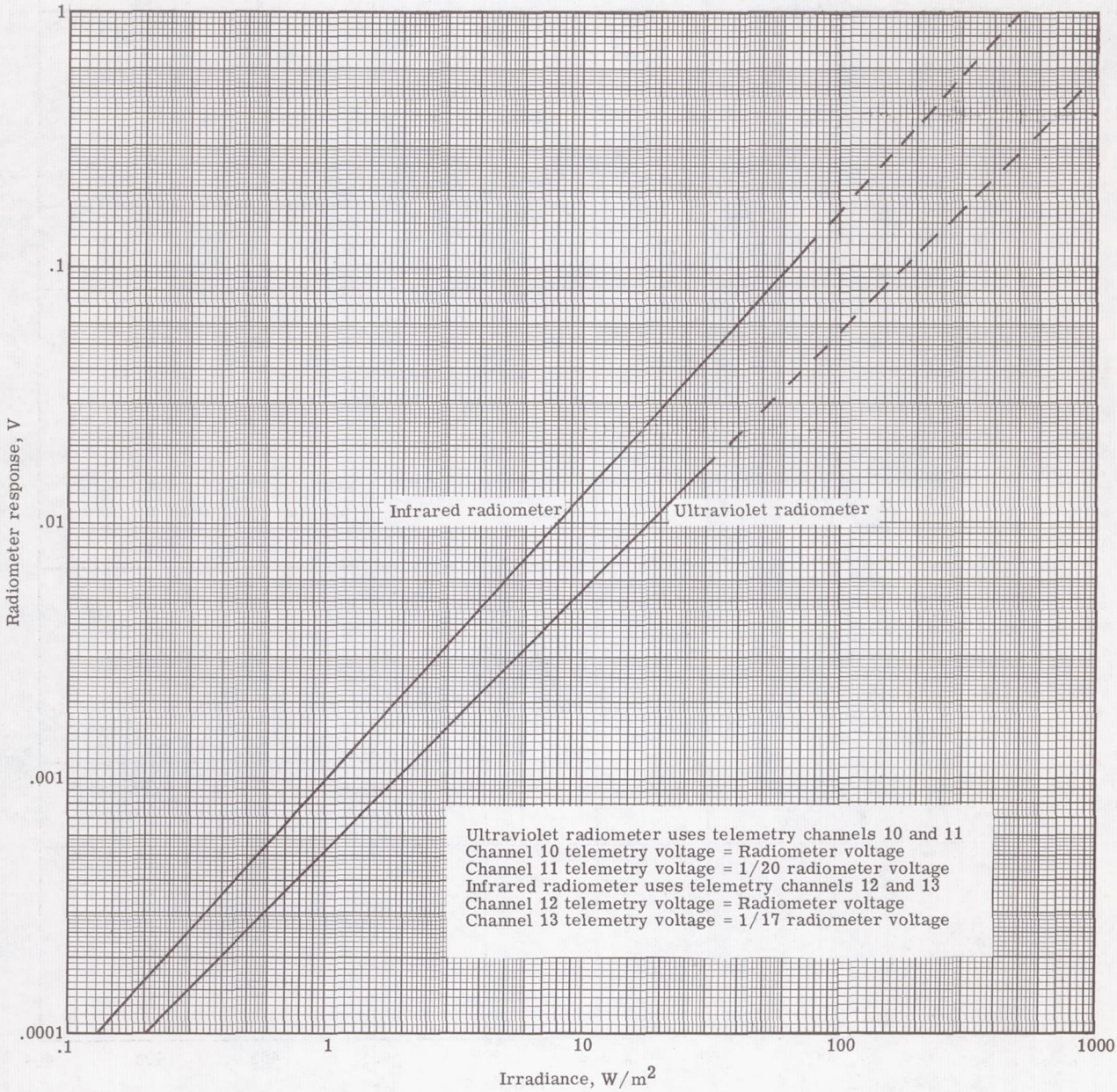

Figure 8.- Radiometer calibrations.

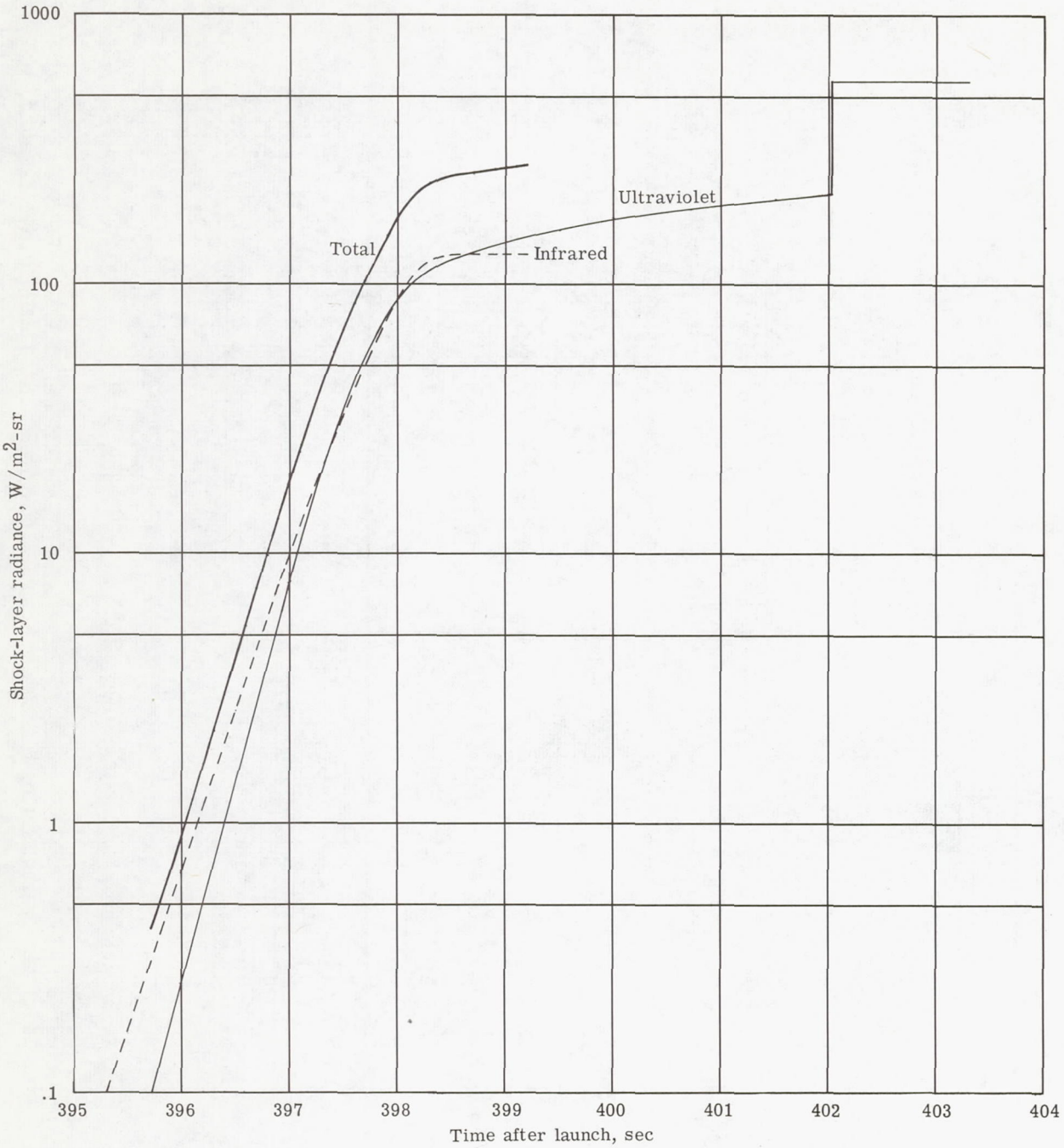

Figure 9.- Radiation measurements.

(2) Calculate the total radiation predicted from the complete nonequilibrium reaction zone (that is, no truncation) of a normal shock wave for the conditions of free-stream density and velocity experienced in flight.

(3) Estimate the radiant-energy density profile in the nonequilibrium zone for a normal shock wave and for a bow shock wave along the stagnation streamline.

(4) Calculate the attenuating effects of truncation of the nonequilibrium zone by the effective protrusion of the body into the shock layer.

(5) Estimate the effects of collision limiting.

Nonequilibrium Spectrum

The spectrum of the nonequilibrium radiation for the conditions of this flight was difficult to predict because of incomplete theory and lack of experimental measurements. Only an estimate of the spectrum could be made by using the few data available (mainly from refs. 8 and 9). The method and rationale used for this estimate are given in appendix B. This anticipated spectrum (fig. 7) was used initially to reduce the flight data. Maximum radiation is predicted in two broad spectral regions, one between 0.25 μm and 0.45 μm and the other between 0.55 μm and 0.95 μm. Minimum radiation is predicted in the main part of the visible spectrum. The two radiometers exhibit good response in the spectral regions where maximum radiation is expected.

The ratio of the sensor outputs is the only indicator of the relative spectrum of the measured radiation that can be obtained with only two broadband measurements. The measurements showed that the ratio of the ultraviolet radiation to infrared radiation was about 1. This ratio agrees with the predicted spectrum (which was based primarily on shock-tube data), so no further refinement of the spectrum was made. Alternately, the ratio disagrees with the postulate that nonequilibrium radiation, like equilibrium radiation, has a very large ultraviolet component. Since the total radiation (ultraviolet plus infrared) does not exceed that predicted by theory (as is shown subsequently), the conclusion that the ultraviolet radiation is not unduly large represents the accomplishment of the experiment's objective. Because in this experiment no evidence was found that the magnitude of the ultraviolet radiation from the shock layer at high altitudes is unusually large, any assessment of the concept of using this part of the optical spectrum for high-altitude detection of noncooperative reentering vehicles by high-altitude aerospacecraft must take this negative result into consideration.

Total Nonequilibrium Radiation

The theory and other experimental measurements (refs. 1 and 8) indicate that an integration of the radiant-energy density over the entire thickness of the nonequilibrium

zone yields a constant value of radiant emittance for a constant velocity. The radiance, that is, radiant emittance per unit solid angle, is then independent of body shape and size and of the free-stream density. This unusual result applies for conditions when binary collisions predominate and when the bow shock wave can be approximated by a one-dimensional normal shock wave. The value predicted (ref. 1, fig. 18) for a flight velocity of 6 km/sec is 4.8×10^3 W/m^2-sr. The flight data, instead of indicating the constant value predicted, show a rapid increase in radiance with time (and free-stream density), and the maximum value obtained at the end of the infrared radiometer's data period is a factor of 20 less than the predicted constant value. Apparently, the bow shock conditions were not proper for experiencing this phenomenon during any part of the flight.

Truncation

Radiation profiles.- Figure 10 illustrates the relative size of the body, light pipes, and bow shock wave. Also illustrated in figure 10 are the radiant-energy density profiles along the stagnation streamline for a bow shock wave and a normal shock wave under the same conditions of ambient density and velocity. The differences observed are attributable to different velocity histories of the particles behind the shock front. Along the stagnation streamline the particle velocity relative to the shock front drops rapidly from maximum at the shock front to near zero at the body. A view along this line shows the nonequilibrium and equilibrium zones. For nonstagnation-point streamlines the particle velocity does not fall so rapidly and the radiation profile approaches that of a normal shock wave. Because of the curvature of these streamlines a view from a radiometer intersects only a fraction of the nonequilibrium zone and misses completely (truncates) the equilibrium zone. A quantitative evaluation of this effect cannot be made without a complete flow analysis, but a blunt body is expected to show less truncation than a pointed body. A pointed body effectively protrudes farther into the shock layer.

As the free-stream density decreases, the relative size of the nonequilibrium zone increases. (The density and temperature conditions change, and the excitation and relaxation processes in the gas last longer.) Consequently, the normal truncation in a bow shock increases to the point where the radiation peak is not reached in the bow region of the body but occurs farther downstream.

Truncation calculations.- Calculations of the predicted degree of truncation for the flight conditions require a knowledge of the following conditions:

(1) The standoff distances of the bow shock wave for the particular body shape and size

(2) The increase in size of the nonequilibrium zone with decreasing density

(3) The radiation profile in the bow region

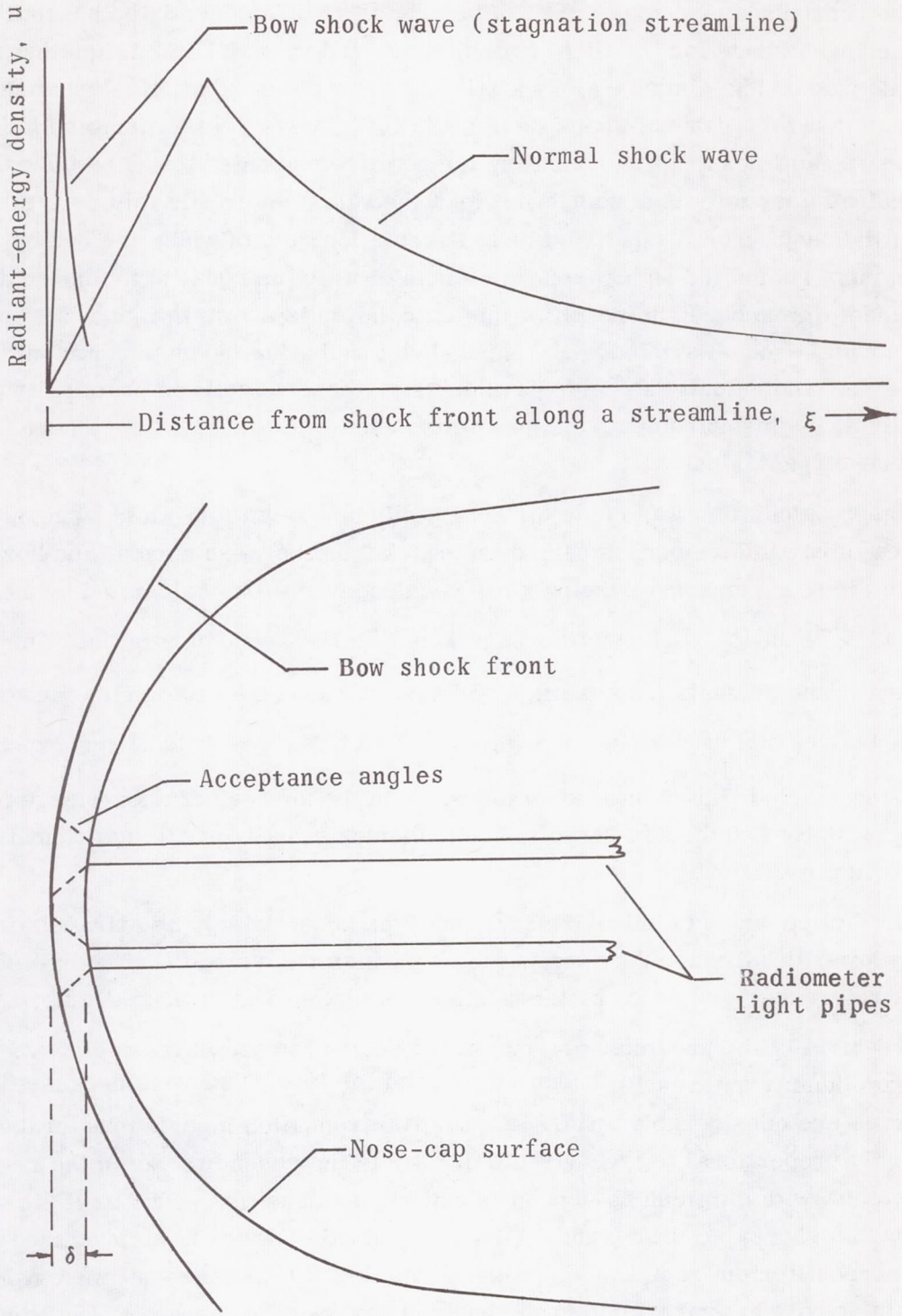

Figure 10.- Comparison of bow and normal shock waves.

A calculation was made by using the shock-standoff-distance theory of references 10 and 11, and the nonequilibrium-zone model of reference 9. (The calculated nonequilibrium shock-standoff distance for the flight conditions varied from 1.1 to 2 times that for the equilibrium case. The distance along a streamline to peak radiation is assumed to be the same as that for a normal shock wave.) No flow analysis was attempted for determining the streamlines and for evaluating the profile segments viewed by the radiometers. Instead a model was assumed in which the radiation profile follows a straight rise from the shock front to the point of peak radiation, and in which the radiometers view a segment behind the shock front the length of which is equal to the nonequilibrium shock-standoff distance. The result of this calculation is shown in figure 11, and is labeled "normal shock-wave model." Shock-layer radiation theories commonly use free-stream density and velocity as basic parameters. Since velocity is practically constant for this flight, the measurements and predictions shown in figure 11 have been plotted against free-stream density.

Another calculation was made for nonequilibrium radiation, which accounted for the differences in particle velocities behind the shock front between normal and bow shock waves. In the bow shock wave the particle residence time was calculated by using the relation $t \approx \frac{0.8r}{V} \ln\left(1 - \frac{\xi}{\delta}\right)$ from reference 12 (V called V_S in ref. 12). The calculation applied to the stagnation streamline and assumed that the radiometer viewed the first three-quarters of this streamline, that is, $\frac{\xi}{\delta} = 0.75$. The result is also shown in figure 11 and is labeled "bow shock-wave model." In the absence of a knowledge of the flow streamlines, these two models serve to bound the analytically predicted truncation of nonequilibrium radiation.

A prediction based on other observations was possible only by extrapolating their results to lower densities and by scaling for body size and velocity. The ballistic-range data from reference 1, adjusted by this method, is also shown in figure 11.

Agreement of the predicted and measured values is good in the region where the free-stream density ratio is 10^{-4}, but not as good for lower densities because the slopes of the curves are considerably different. The two truncation models predict the radiation to be roughly proportional to free-stream density to the second power in the region of the measurements, with diminishing dependence at higher densities. The ballistic-range measurements show a similar trend. (Without truncation there is no predicted dependence of nonequilibrium radiation on free-stream density, and the equilibrium radiation varies with density to approximately the one and seven-tenths power.) The flight measurements, however, show that the radiation is proportional to free-stream density to greater than the third power, which indicates an additional density-dependent process.

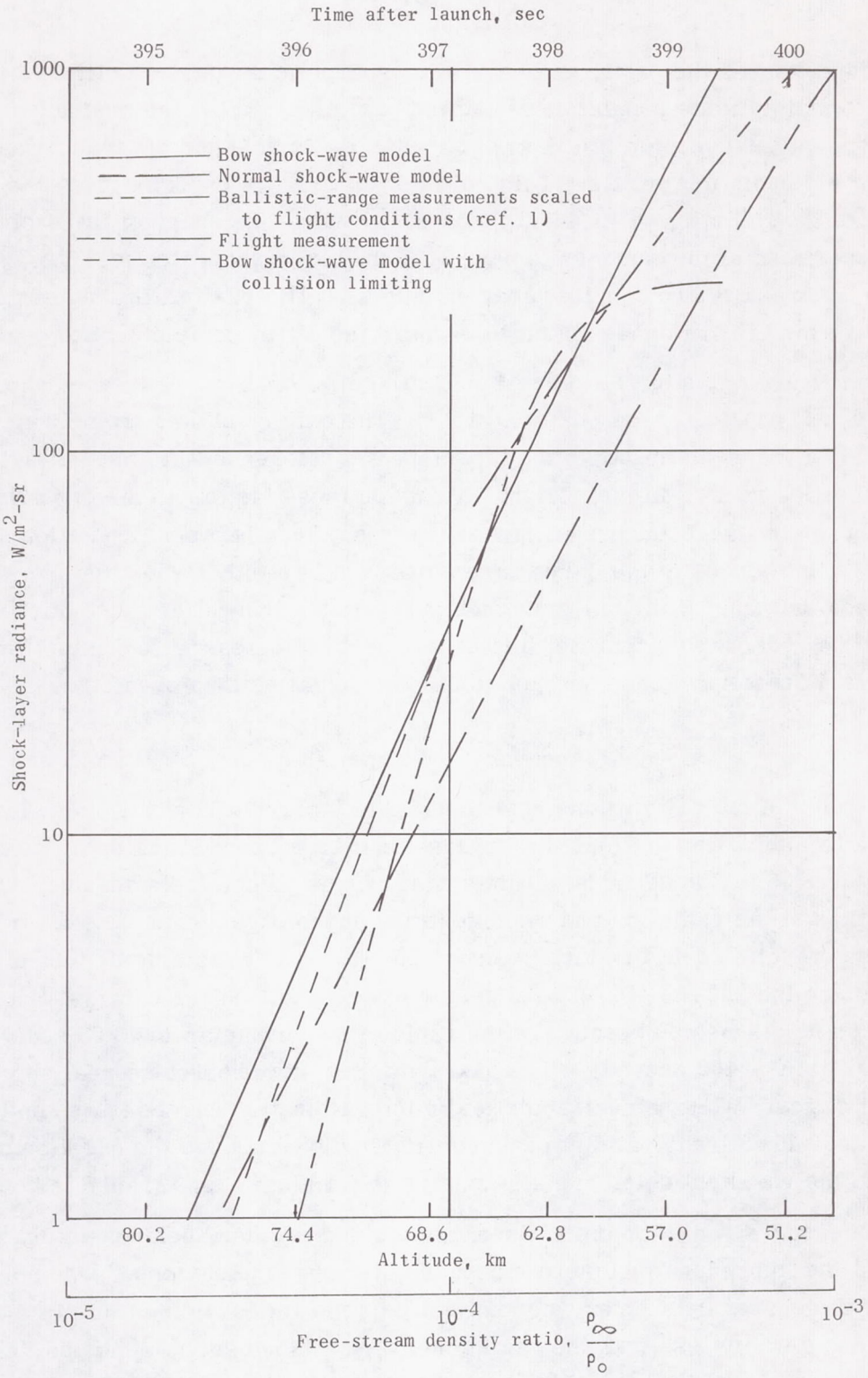

Figure 11.- Comparison of flight data to predictions.

Collision Limiting

At low densities the particles become too sparse to produce a sufficient number of collisions to maintain the population of excited particles against the drainage by radiation. This effect is called collision limiting, and it effectively changes the truncation process by changing the radiation profile. This collision limiting is expected, first, to reduce the peak value of the radiation profile and, second, to change the shape of the profile. Because experimental measurements have been unable to separate these two changes in the profile, the results are usually reported only as collision-limiting factors, which vary from 1 where the effect is nonexistent to 0 where the effect completely stops all radiation.

The measurements of reference 1 indicate collision-limiting factors should be less than 1 for density ratios of less than 2×10^{-5}. The empirical data from Project Fire were used, in a manner similar to that described in reference 2, to predict actual collision-limiting factors for this flight. By using these factors to modify the bow shock-wave truncation in figure 11, better agreement is obtained between prediction and experiment, that is, the slopes of the curves are more nearly equal. When the shock-standoff distances and the nonequilibrium-zone sizes used in the truncation calculations are assumed to be reasonably accurate, this experiment indicates that collision limiting for this flight is more severe and continues to higher densities than predicted.

Accuracy and Anomalies

The radiometric calibrations repeated within 5 percent, and the overall uncertainty in the measurements was estimated to be less than 25 percent in the data period from approximately 396 to 398 seconds. This accuracy was judged to be adequate for the dynamic range of the radiation and the objectives of the experiment. However, the experimental results could be more useful if the ultraviolet radiometer (channel 11) data obtained during the 398- to 402-second period were valid. These data were not included in the preceding discussion because of the rapid slope change around 398 seconds and the abrupt saturation at 402 seconds. The data, however, may represent real shock-layer radiation changes. When the extrapolation in the calibration curves is assumed to be valid (see appendix A), the validity of these data revolves around the question of light-pipe melting and the resultant deleterious effects of self-radiation and transmission losses.

The measured radiation did not seem to include an added component due to thermal radiation of the light pipes themselves because the surrounding copper was not hot, and very likely the quartz light pipes were not hot, and the radiation from melting quartz would be considerably less than the values measured. (See section entitled "Environmental Testing" in appendix A.) However, the shock-layer radiation transmitted through the light pipes could be attenuated significantly by a sufficiently thick layer of melted quartz. The abrupt loss of such a molten layer could account for the sudden rise in the

output of the ultraviolet radiometer at 402 seconds. Accurate simulation of this effect is not possible, so that the question remains unresolved. Because of the simplicity of the measurement technique used in this flight, it may be applicable to other reentry experiments for which more accurate simulation of the environment and the performance of the light pipes may be desirable.

SUMMARY OF RESULTS

This experiment provided a look at the stagnation-point radiation from a reentry body at extremely high altitudes. The reentry body configuration and the reentry velocity allowed observations of nonequilibrium radiation effects not previously measured in flight. The experiment results, therefore, complemented those from Project Fire and those from ground-based investigations and can be applied to the problem of reentry heating and to the evaluation of the concept of optically detecting and tracking noncooperative reentry vehicles. The following general conclusions may be drawn:

1. The measurements verify the overall shock-layer radiation levels predicted by nonequilibrium theory.

2. In the stagnation region the contribution that the ultraviolet makes to the total radiation is not large.

3. For nonblunt bodies the truncation of the radiation by projection of the body into the shock layer is within the bounds of the analytical predictions for free-stream density ratios greater than 10^{-4}.

4. Radiation limiting caused by the sparsity of binary collisions at high altitudes (low densities) appears to be at least as significant as that predicted by theory and other measurements.

5. The measurement technique used, because of its simplicity, may be applicable to other reentry experiments.

Langley Research Center,
National Aeronautics and Space Administration,
Langley Station, Hampton, Va., September 9, 1968,
125-24-01-11-23.

APPENDIX A

MEASUREMENT SYSTEM

This appendix presents some detailed information on the fabrication, environmental testing, and calibration of the measurement system. This information should aid in the understanding of the experiment results, as well as in the evaluation of this simple and compact radiometric method as a possible technique for other applications in severe environmental conditions similar to that of reentry.

Figure A-1 shows a cutaway diagram of the radiometer. The radiometer was designed as an integral part of the reentry nose cap. The stagnation-point radiation was transmitted by solid fused-quartz light pipes to two sensors. One sensor was a silicon planar photodevice sensitive to the infrared radiation; the other sensor was an antimony-cesium photoemissive diode sensitive to the ultraviolet radiation. Their response times were better than adequate for the purpose. Appropriate electrical networks, including a direct-current amplifier, were used to match the sensors to the encoder (input impedance is 1000 ohms; input levels are from 0.5 mV to 20.0 mV). In order to increase the dynamic range of the measurements, the signals from each sensor were fed into two encoder channels with different sensitivities where they were sampled 45 times per second.

Fabrication

Electrolytic tough-pitch oxygen-free copper was used for the nose cap which was polished to a finish with less than 2 microinch root-mean-square roughness. The 1-mm-diameter light-pipe holes were drilled 60 mm through the copper nose cap by using aircraft extension-type drills with very accurate and sharp cutting edges. Precise alinement and controls were required to insure that the drilling did not deviate from the intended path. The light-pipe holes pass from the copper through a glass-filled phenolic block, which required the same drilling precision.

The glass-filled phenolic block was press fitted to the copper nose cap. A nylon collet-type chuck secured the light pipes in the phenolic block. The fused-quartz light pipe was selected and fitted to the individual nominal 1-mm holes with a minimum clearance, estimated to be less than 0.0025 mm. The light pipes were removed, cut to length, polished on both ends, and the part to be clamped by the collet was aluminized to prevent light leakage to the collet. Before final assembly, all parts were cleaned thoroughly so that no foreign agents could wet the sides of the light pipes and, thereby, reduce their transmittance. (Care was always taken to prevent dust, moisture, and so forth from affecting the pipes.)

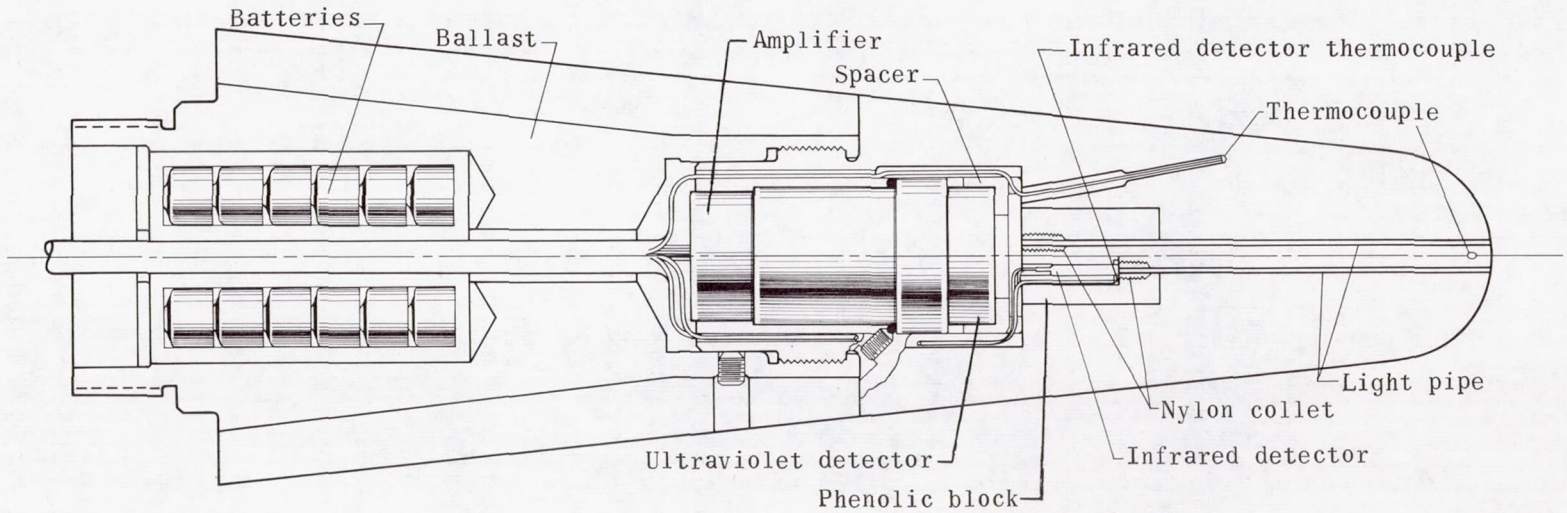

Figure A-1.- Radiometer system in nose cap.

APPENDIX A

The silicon (infrared) detector was 2 mm in diameter and 1.5 cm long and its sensitive area measured 0.6 mm by 0.7 mm. The photoemissive (ultraviolet) detector was vacuum-packed in a stainless-steel shell 2.85 cm in diameter by 4.45 cm long with a sapphire window. The sensitive area of the detector was 10 mm in diameter. The light pipes were positioned so that the radiation covering their acceptance angles filled the sensitive areas of the detectors to minimize sensitivity shifts. The spectral transmission and acceptance angles of the light pipes and the spectral response of the sensors were checked before and after installation to insure that the performance did not deteriorate.

Two platinum—platinum—10-percent-rhodium No. 30 thermocouples (0° to 1760° C), measured the temperature of the copper nose cap. One thermocouple, 0.25 cm from the stagnation point, monitored the temperature in the vicinity of the light-pipe surfaces; another, 6 cm from the tip of the nose cap, monitored the heat-transfer rate. Both thermocouples were installed with metal sheaths and were silver-soldered in place.

The matching amplifier was assembled in a package, 2.5 cm in diameter by 1.6 cm in height. Final adjustments were made for the zero and gain, and for the unit sealed and attached directly to the ultraviolet sensor.

A photograph of the radiometer parts before assembly is shown in figure A-2.

Calibration

The radiometer was calibrated for absolute spectral response, solid-angle response, and linearity by using the setup sketched in figure A-3. Spectral calibration for the ultraviolet sensor covered a range from 0.25 μm to 0.60 μm when using a high-intensity mercury lamp as a source. (See graph of spectrum in fig. A-4.) The strong lines in the mercury spectrum were used as points of wavelength calibration. The infrared sensor was calibrated from 0.5 μm to 1.2 μm by using a standard tungsten source. Since the tungsten source was a continuum, wavelength calibration points at 0.1-μm interval were used. Both ultraviolet and infrared monochrometers were set for 100 Å bandwidth for the spectral calibrations. Although the spectral irradiances of the lamps were known, the complete calibration system responses were not known; therefore, a standard thermopile was used to measure the energy in each spectral bandwidth. The sensitive area of the thermopile was placed at the same point as the light pipes and viewed the same radiating surface. Since the acceptance angles of the radiometers were greater than the solid angle of the monochrometer, a diffuser was inserted in the output of the monochrometer to fill the radiometer field.

The size of the source (diffuser) was controlled by an iris assembly, and the relative response of the radiometer was plotted against the solid angle (computed from the known geometry of the system). These results are given in figure 5. The higher

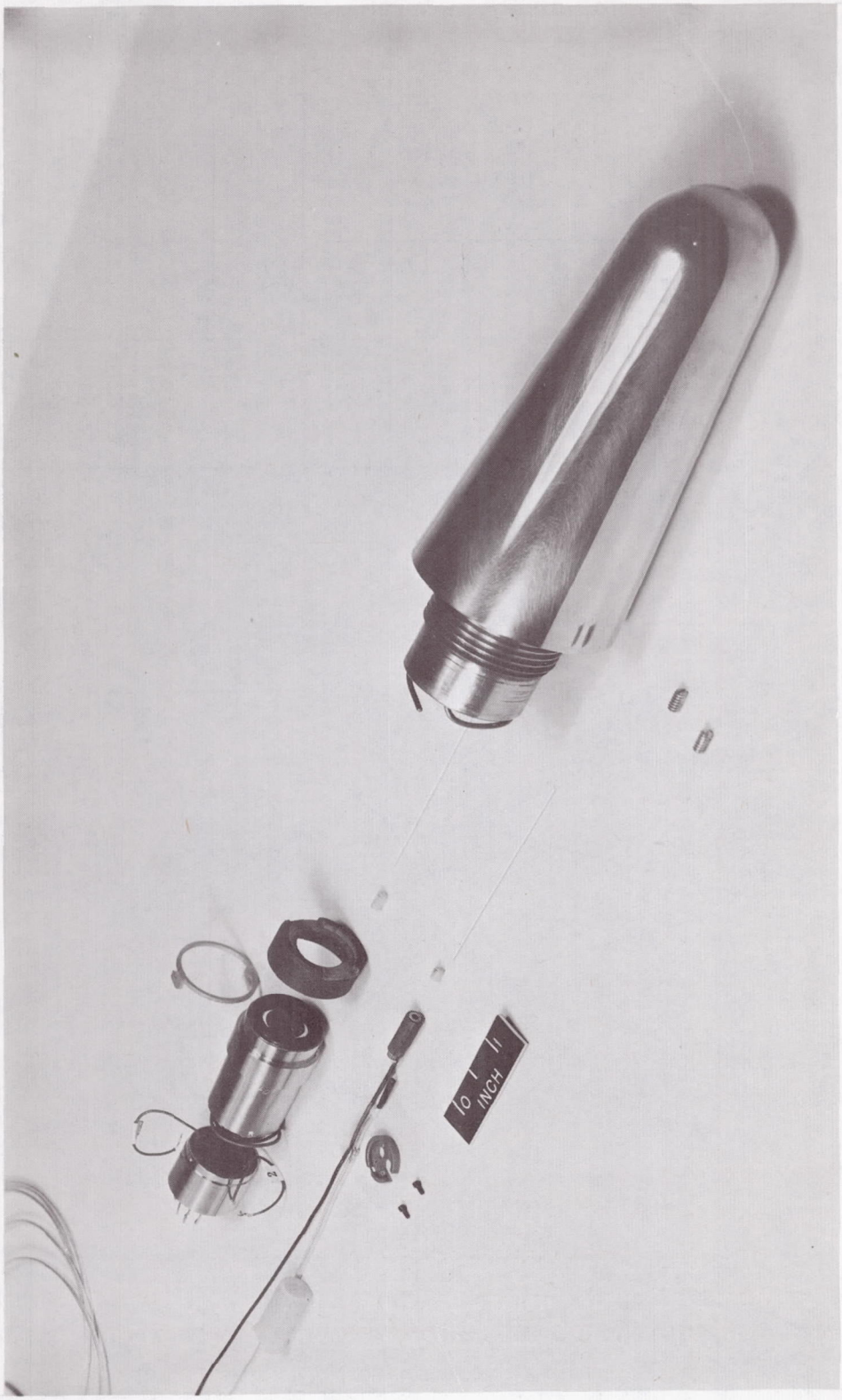

L-63-6621

Figure A-2.- Radiometer parts before assembly.

APPENDIX A

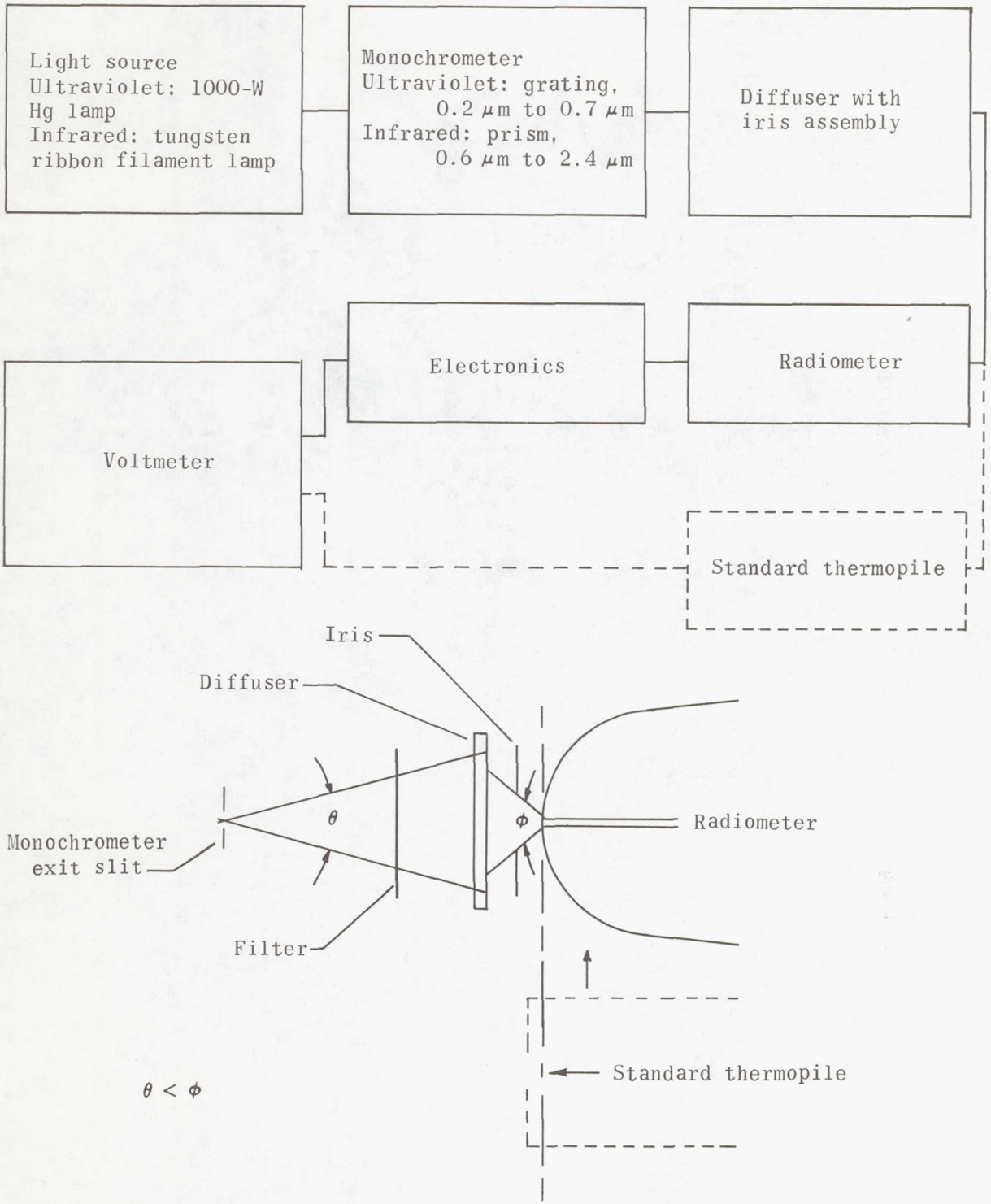

Figure A-3.- Calibration setup.

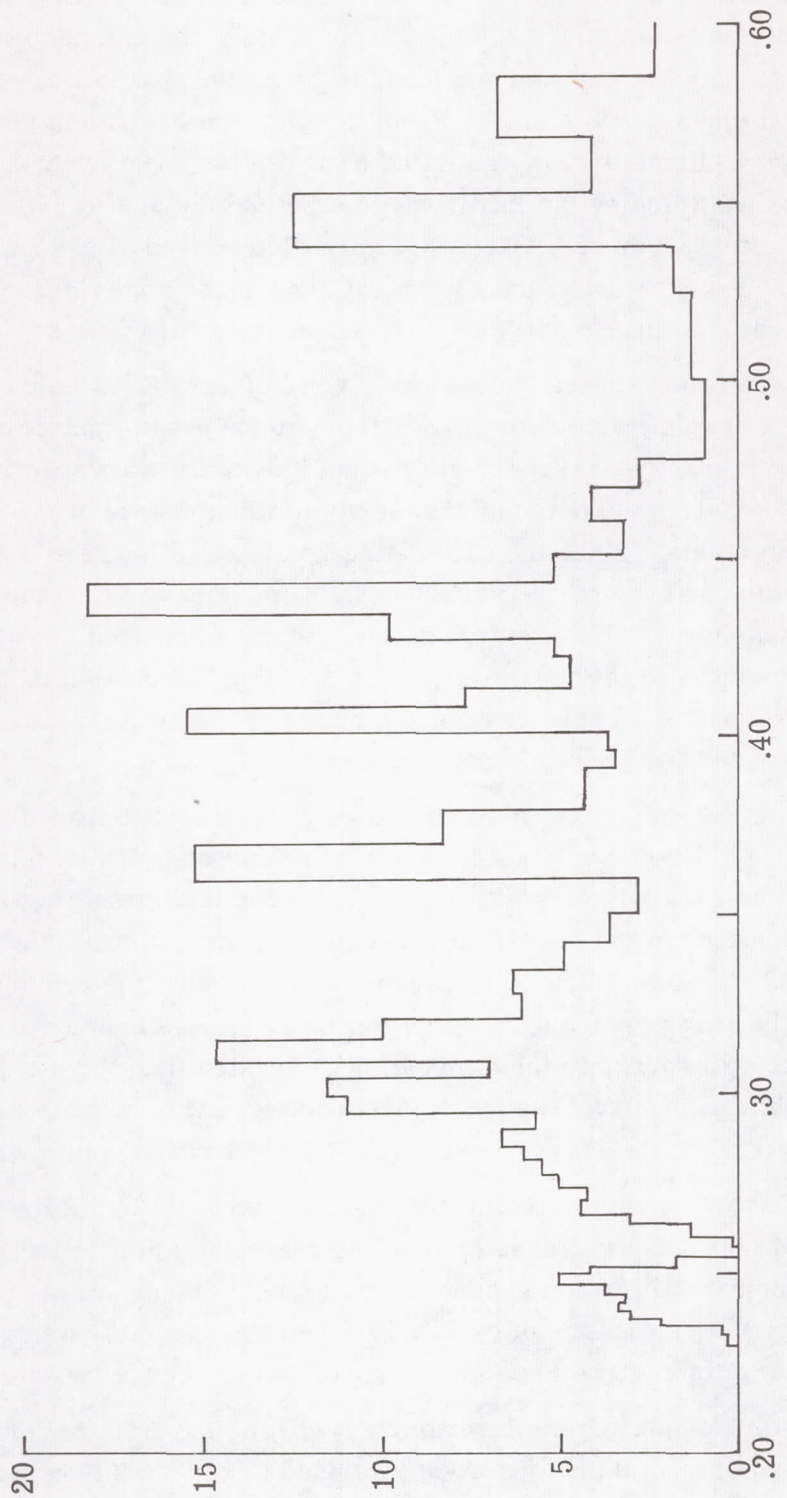

Figure A-4.- Spectrum of high-intensity mercury lamp.

response at small solid angles exhibited by the ultraviolet radiometer is typical for a photoemissive cathode, as is the plateau in the response after the cathode is completely covered. (The light pipes were checked and found to be responsive to larger solid angles than allowed by the radiometer geometry.) From the plot, the equivalent acceptance angle of the ultraviolet radiometer was estimated to be 1.5 sr. The lower response at the small solid angles exhibited by the infrared radiometer was caused by the offcenter positioning of the sensitive element. This positioning also caused a less rapid leveling at large solid angles. From the plot, the equivalent acceptance angle of the infrared radiometer was estimated to be 1.6 sr.

The absolute spectral-response curves are given in figure 6. The average response over the spectral band of each radiometer was obtained by averaging the point-by-point products of the absolute spectral-response curves and the anticipated spectrum. (See fig. 7.) The calibration constants obtained thus apply for light levels of the same magnitude as the calibrating levels. Since the calibrating levels were low, the zeroth order of the monochromator was used to provide sufficient light to check the linearity of the radiometers to much higher levels. Neutral density filters were used to reduce the light levels in several steps down to the level used in the spectral calibration to provide the necessary absolute reference. These results are shown in figure A-5; the same curves converted from neutral density to irradiance are shown in figure 8.

Much difficulty was experienced in calibrating the neutral density filters in the ultraviolet band. Screen filters could not be stacked without complex fringing problems; and inconel filters varied sharply with wavelength and made it impossible to evaluate accurately the contributions of the strong spectral lines in the calibrating source. Since the electrical components of the ultraviolet radiometer, including the photoemissive detector, are basically linear over a wide operating range, it was concluded that, beyond a neutral density of 0.5, the error in the calibration is greater than the nonlinearity of the radiometer. The calibration curve was drawn accordingly. The infrared radiometer is characteristically nonlinear; therefore, a best fit to the calibration points was used.

The dashed-line parts of the curves represent the extrapolation of the curves to levels anticipated in flight that were greater than those available for calibration. The points of absolute spectral calibration chosen for referencing these curves to an irradiance scale were taken near the maximum spectral calibration levels. Neutral density was then converted to watts/meter^2 to produce the calibration curve shown in figure 8.

Immediately after completing the laboratory calibration, a field calibrator, employing a small tungsten lamp (see fig. A-6) was used to record the output from the sensors for a specified lamp current. These records were then used as a standard for final calibrations after assembly to the launch vehicle. The field calibration device utilized the same neutral density filters for the linearity checks as were used in the

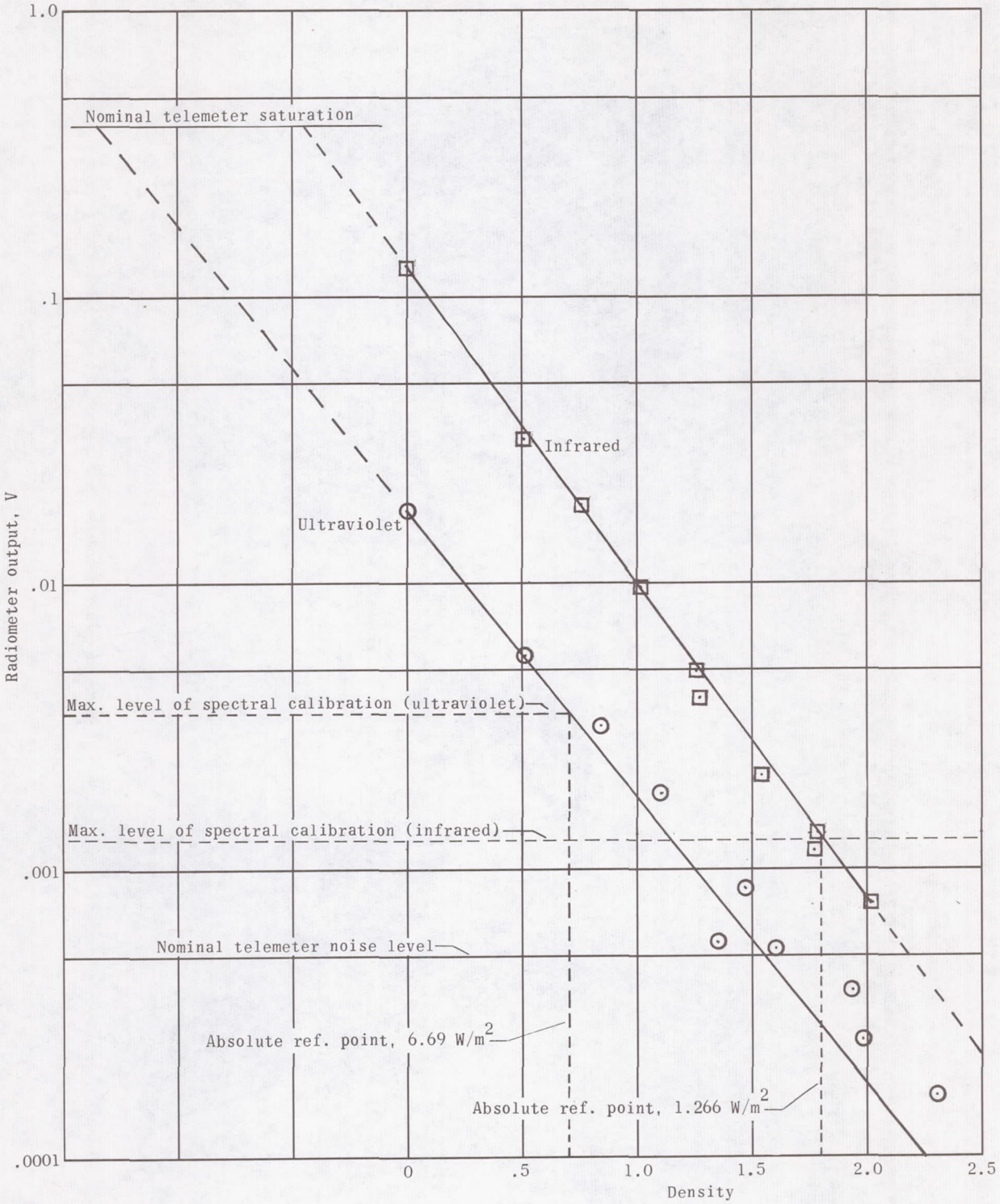

Figure A-5.- Radiometer calibrations.

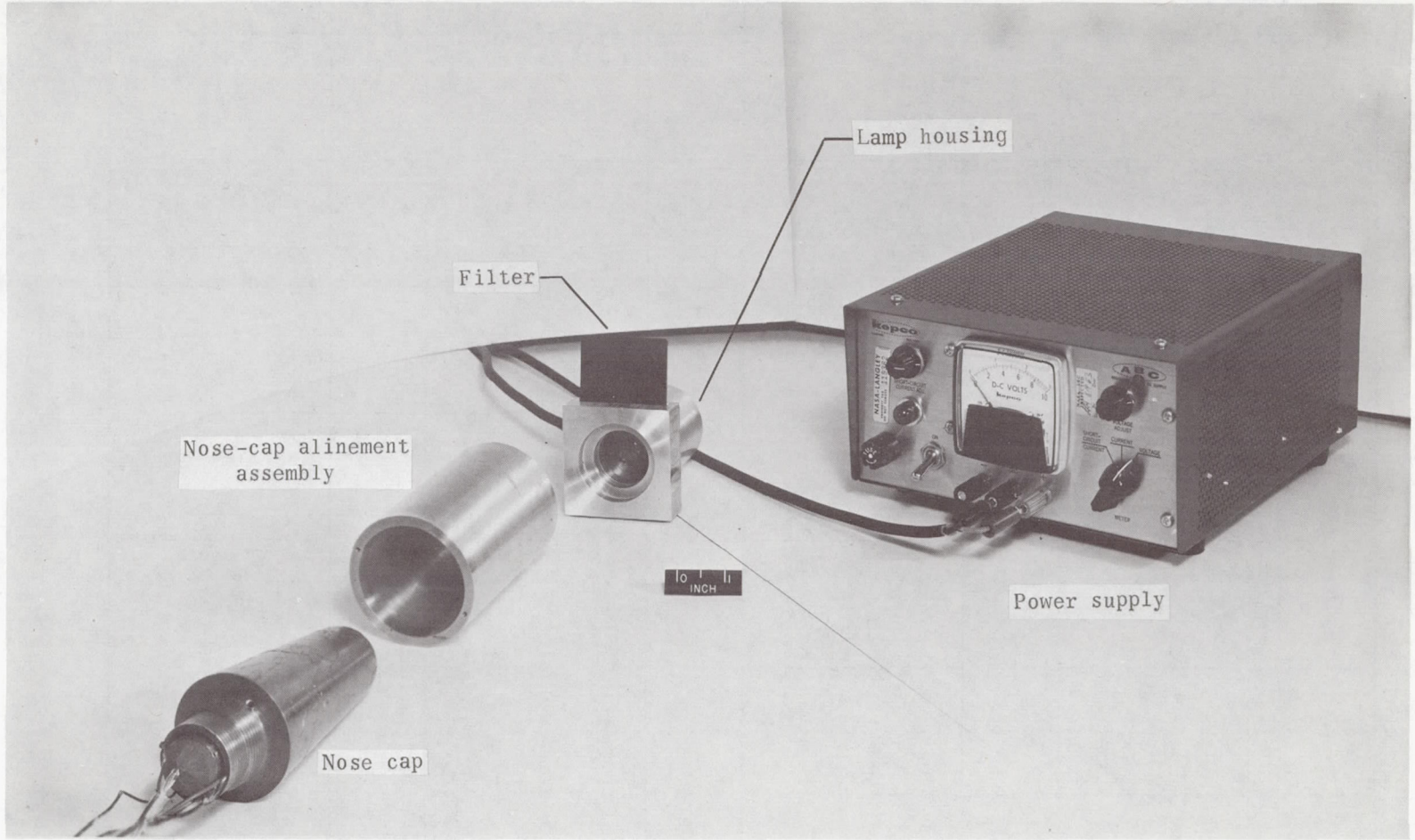

Figure A-6.- Field calibrator.

L-63-6622.1

laboratory calibration. The spectral response was checked by using color filters centered at 0.52 μm for the ultraviolet channel and 0.93 μm for the infrared channel.

Environmental Testing

All components were tested for the anticipated environmental conditions. In addition, some special testing was done. The light pipes were tested for thermal shock and for transmission at elevated temperatures. The thermal-shock tests used larger specimens than the light pipes and were considered conservative because the larger pieces were more likely to fracture under thermal shock. A piece of fused quartz (0.5 mm by 20.0 mm by 50.0 mm) was immersed in liquid nitrogen (-196^{o} C) and then into molten copper (1082^{o} C). Neither this piece nor pieces as large as 6.4 mm in diameter by 100.0 mm long fractured. Additional thermal tests on the windows were conducted in the electric arc facilities (2 W/cm^2) and the ceramic-heated jet (300 W/cm^2) at the Langley Research Center where the only damage that occurred was due to sand blasting by particles in the ceramic heater. In the clean electric arc facilities the evidence indicated that the quartz did not reach the molten state.

The transmission of the light pipes with melting exposed surfaces was simulated by measuring the spectral transmission against temperature of two 1.5-mm-thick-quartz plates sandwiching a thermocouple. As the temperature indicated by the thermocouple was raised from room temperature to 1650^{o} C by heating with a torch, the transmission was monitored by using a monochrometer and a photometer. Surface melting began when the thermocouple indicated approximately 1400^{o} C. The average decrease in transmission over the ultraviolet band was in the order of 50 percent at the highest temperature. The change in transmission at the longer wavelengths was much less. With the intense source used for the test, there was no indication of an error contribution from the self-radiation of the quartz at its temperature.

The matching amplifier required temperature compensating components which were aged and cycled by testing this unit separately from 0^{o} C to 50^{o} C. The drift in output was less than 1 mV, and the linearity change with temperature was negligible.

The environmental tests were performed on two radiometer systems (flight and backup) after they were assembled and calibrated. A list of test specifications is given in table A-I. After the environmental tests were performed, the radiometer was recalibrated and showed no change.

APPENDIX A

TABLE A-I.- ENVIRONMENTAL SPECIFICATIONS

Type of test	Test specifications	
	Thrust direction	Normal and transverse
Steady-state acceleration:		
Positive:		
Level, g units	150	15
Duration, min	3	3
Attachment	Nose toward center of centrifuge, mounting to apply thrust through empty 38.1-cm solid-rocket motor with inert loaded 12.5-cm solid-rocket motor in place	To simulate attachment to 38.1-cm solid-rocket motor with inert loaded 12.5-cm solid-rocket motor in place
Negative (exit):		
Level, g units	42	----------
Duration, min	3	----------
Shock:		
Positive only:		
Level, g units	90	----------
Duration, msec	5 to 10	----------
Shape	Square (approx.)	----------
No. of shocks	2	----------
Vibration:		
Frequency range, Hz	20 to 2000	20 to 2000
Level, g vector	±1	±1
Sweep speed, octaves/min	4	4
Sweep setting, deg/min	90	90
Duration, sec	96	96
Sinusoidal (normal):		
First frequency band, Hz	20 to 200	20 to 200
Level, g vector	±1	±1
Second frequency band, Hz	200 to 500	200 to 500
Level, g vector	±3	±3
Third frequency band, Hz	500 to 2000	500 to 2000
Level, g vector	±5.5	±2.5
Sweep speed, octaves/min	4	4
Sweep setting, deg/min	90	90
Duration, sec	96	96
Sinusoidal (narrow band):		
Frequency band, Hz	550 to 560	550 to 650
Level, g vector	±15	±2.5
Sweep setting, deg/min	18 (180 × 0.1)	18 (180 × 0.1)
Duration, sec	18	18
Random:		
Frequency band, Hz	20 to 200	20 to 2000
Level, spectral density, g^2/Hz	0.036	0.018
Level, g rms	8.5	6
Duration, sec	96	96

APPENDIX B

RADIATION PREDICTIONS

Equilibrium Radiation

The radiation from the equilibrium zone of a shock wave in air comes from several species, the contributions of which vary with the density and temperature in the shock layer. Aerodynamic charts and tables are available (ref. 4) from which these quantities can be obtained for various altitude-velocity histories. The corresponding equilibrium-species composition is also well-known. Unfortunately, because quantitative determination of the emittance from each species is difficult, empirical parameters are used. An empirical rule (which approximates the average results from the theories of refs. 5 to 7) states that the total equilibrium radiant emittance per unit shock-layer thickness varies as the shock density to the one and three-tenths power and the shock temperature to the twelfth power. If the velocity is constant, the emittance varies with density to the one and seven-tenths power. The corresponding spectral distribution as a function of density is practically constant. Figure B-1 shows the predicted spectrum for the flight velocity at an altitude of 35 km. For a first approximation of the equilibrium radiation for the flight, a constant velocity of 6 km/sec is assumed, and the corresponding relation used for the radiant emittance per unit shock-layer thickness is $u = 10^3(\rho/\rho_0)^{1.7}$. Then the total radiant emittance from the shock layer is predicted by assuming an optically thin gas and by multiplying the radiant emittance per unit shock-layer thickness by the thickness of the complete shock layer. This thickness, the shock-standoff distance, is a function of the altitude-velocity history and the size of the body (refs. 10 and 11). For a small spherical body with a velocity of 6 km/sec, the shock-standoff distance is approximated by $\delta = 0.75r\,\frac{\rho_\infty}{\rho}$.

Values of the total radiant emittance calculated by this method are an order of magnitude below those measured in the flight and exhibit a weaker density dependence than do the flight data. Furthermore, there was no evidence in the flight data of the sizable ultraviolet component predicted by equilibrium theory. Therefore, the equilibrium radiation was negligible for this flight measurement.

Nonequilibrium Radiation Spectrum

The literature provided very little information on the nonequilibrium radiation spectrum to expect from this flight. In using the available data, it was difficult to know when it applied to the flight case. Some reasons for this difficulty are as follows:

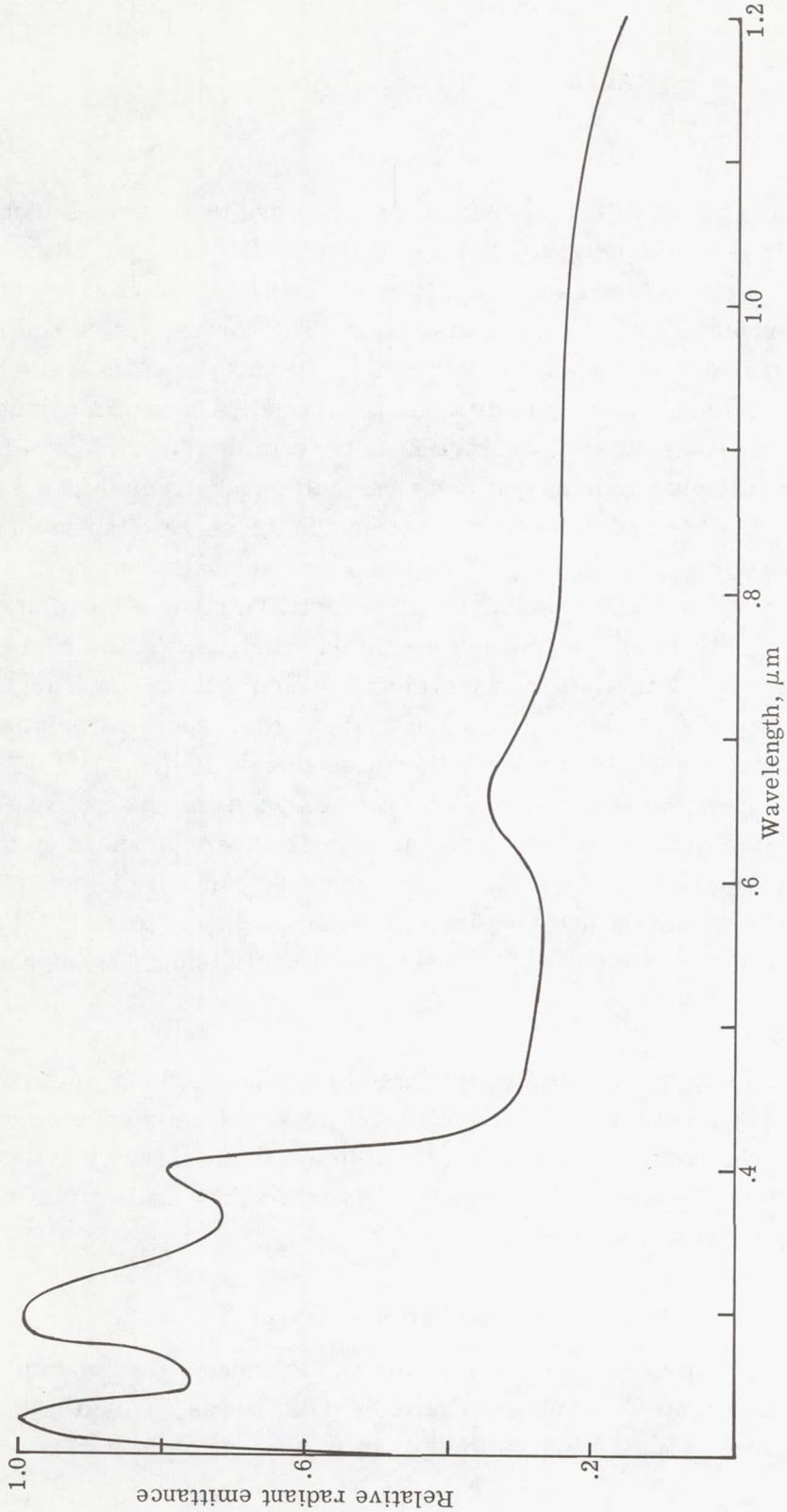

Figure B-1.- Spectrum predicted by equilibrium theory.

APPENDIX B

(1) Normalizing the data at the peaks gives trouble because in shock tubes these peaks are caused by impurities not experienced in flight.

(2) The strong radiation at 0.8 μm to 0.9 μm is evident at a velocity of 10 km/sec, but is expected to be less pronounced at lower velocities.

(3) Determining what is scatter and what is real data cannot be done with such small quantities of data representing such large ranges of experimental conditions.

The available data (mainly from refs. 8 and 9) are plotted in figure B-2. The curve defining the trend of the data is, at best, a rather crude estimate and is the one used to reduce the flight data. This curve was also shown in figure 7. The check on the spectrum (ratio of ultraviolet to infrared) indicated that it was not grossly in error. The spectrum was later compared to the recently available Project Fire data (ref. 13). The Fire data exhibited a similar overall spectrum at the very high altitudes, and showed some of the line and narrow-band features. However, the large disparity in the body sizes and the reentry velocities of the two experiments precluded use of the Fire data to refine the spectral estimate for this flight.

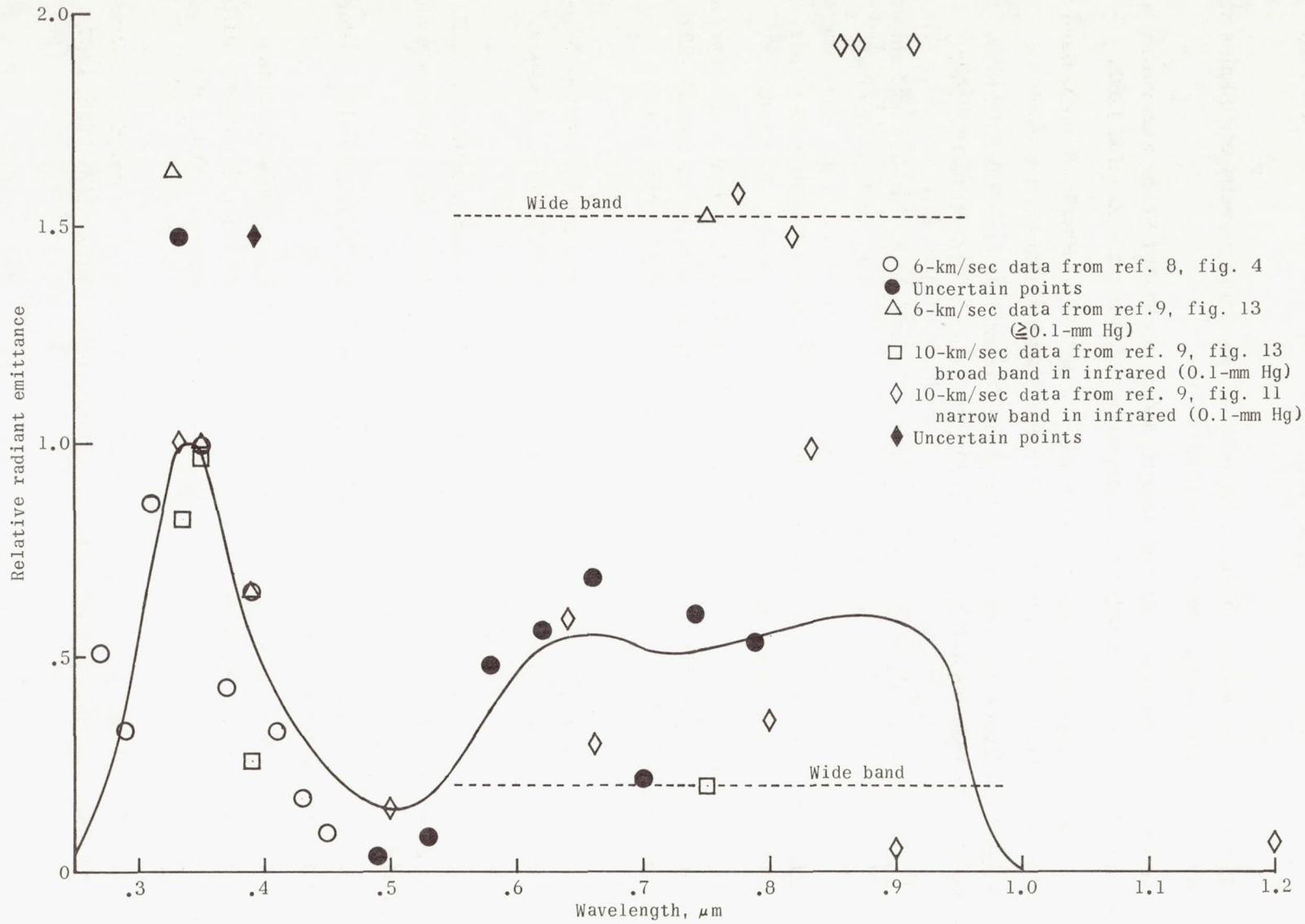

Figure B-2.- Spectrum estimated from nonequilibrium measurements and theory.

REFERENCES

1. Page, William A.; and Arnold, James O.: Shock-Layer Radiation of Blunt Bodies at Reentry Velocities. NASA TR R-193, 1964.

2. Cauchon, Dona L.: Radiative Heating Results From the Fire II Flight Experiment at a Reentry Velocity of 11.4 Kilometers Per Second. NASA TM X-1402, 1967.

3. Kendall, Bruce M.; and Harrington, Richard F.: Flight-Test Results of an X-Band Telemetry System on a Trailblazer II Vehicle. NASA TM X-1474, 1967.

4. Huber, Paul W.: Hypersonic Shock-Heated Flow Parameters for Velocities to 46,000 Feet Per Second and Altitudes to 323,000 Feet. NASA TR R-163, 1963.

5. Kivel, B.; and Bailey, K.: Tables of Radiation From High Temperature Air. Research Rept. 21 (Contracts AF 04(645)-18 and AF 49(638)-61), AVCO Res. Lab., Dec. 1957.

6. Meyerott, R. E.; Sokoloff, J.; and Nicholls, R. W.: Absorption Coefficients of Air. GRD-TR-60-277 (Geophys. Res. Papers No. 68), U.S. Air Force, July 1960.

7. Nardone, M. C.; Breene, R. G.; Zeldin, S. S.; and Riethof, T. R.: Radiance of Species in High Temperature Air. Tech. Inform. Ser. R63SD3 (Contract AF 04(694)-222), Missile and Space Div., Gen. Elec. Co., June 1963. (Available from DDC as AD No. 408564.)

8. Camm, J. C.; Kivel, B.; Taylor, R. L.; and Teare, J. D.: Absolute Intensity of Nonequilibrium Radiation in Air and Stagnation Heating at High Altitudes. J. Quant. Spectry. & Radiative Transfer, vol. 1, no. 1, Sept. 1961, pp. 53-75.

9. Allen, R. A.; Rose, P. H.; and Camm, J. C.: Nonequilibrium and Equilibrium Radiation at Super-Satellite Re-Entry Velocities. Paper No. 63-77, Inst. Aerospace Sci., Jan. 1963.

10. Van Dyke, Milton D.; and Gordon, Helen D.: Supersonic Flow Past a Family of Blunt Axisymmetric Bodies. NASA TR R-1, 1959.

11. Katzen, Elliott D.; and Kaattari, George E.: Flow Around Blunt Bodies Including Effects of High Angles of Attack, Nonequilibrium Flow, and Vapor Injection. AIAA Entry Technology Conference, CP-9, Am. Inst. Aeron. Astronaut., Oct. 1964, pp. 106-117.

12. Nealy, John E.: Models for the Analysis of CN Violet Radiation Behind Shock Waves in Air Contaminated With Carbon-Bearing Compounds. NASA TN D-3935, 1967.

13. Cauchon, Dona L.; McKee, Charles W.; and Cornette, Elden S.: Spectral Measurements of Gas-Cap Radiation During Project Fire Flight Experiments at Reentry Velocities Near 11.4 Kilometers Per Second. NASA TM X-1389, 1967.

NASA-Langley, 1968 —— 33 L-6125